

Sn/Ce co-doping of TiO₂ nanoparticles: influence of dopants concentration on optical and structural characteristics

Behzad Koozegar Kaleji¹ · Mahnaz Alijani¹ · Alireza Aghaei²

Received: 28 January 2016 / Accepted: 19 April 2016 / Published online: 23 April 2016
© Springer Science+Business Media New York 2016

Abstract In this study, different samples of Sn and Ce co-doped TiO₂ nanoparticles (0.5–1–2 mol% Ce and 1–5–10 mol% Sn) were prepared via simple sol–gel synthesis method by using cerium nitrate hexahydrate as cerium precursor, Tin(II) chloride dehydrate as Tin precursor, and titanium (IV) butoxide (TBT) as titanium precursor. The effects of co-doping on the structural, optical, and photocatalytic properties of nanoparticles were studied by X-ray diffraction (XRD), Field emission SEM (FE-SEM), TEM and UV–Vis absorption spectroscopy. Surface chemical state of nanoparticle was thoroughly examined by atomic X-ray photoelectron spectroscopy (XPS). XRD results showed that, titania rutile phase formation in ternary system (Ti–Ce–Sn) was inhibited by Ce⁺⁴ and promoted by Sn⁺⁴ co-doped samples at higher percentage of Sn (5, 10 %). The prepared co-doped TiO₂ photocatalyst nanoparticles showed optical absorption edge in the visible light region and exhibited excellent photo-catalytic ability for degradation of methylene blue (MB) solution under visible irradiation. Sn/Ce co-doped TiO₂ showed higher catalytic activity under visible light irradiation. Visible photo-catalytic activity of Sn/Ce co-doped TiO₂ was obviously higher than that of pure TiO₂ and reached the maximum at Ce and Sn contents of 2 and 5 mol%, based on MB dye decomposition rate.

1 Introduction

Titanium oxide is a well-known photocatalyst working in the ultraviolet (UV) region of light with a band gap of 3.2 eV. Numerous reports are available regarding the shifting of wavelength corresponding to the onset of absorption from UV to visible region of light in TiO₂ as a consequence of doping with cationic or anionic dopants. In the studies employing Ce doped TiO₂ in powder form, Ce doping was reported to enhance the photocatalytic activity of TiO₂ powder, when used <0.5 %. The positive effect of Ce and also of other dopants was suggested as decreasing the particle size and increasing the surface area of powders, thus providing higher adsorption; introducing new electronic states into the band gap of TiO₂, and separation of the charge carriers [1–3]. Co-doping of TiO₂ with Ce and other elements such as Fe [4] or Si [5] was reported to further increase the photocatalytic activity when used in proper amounts.

Doping TiO₂ with antimony and chromium results in the shifting of absorption band from UV to visible light region and exhibits photo-catalytic activity for O₂ generation from aqueous silver nitrate solution under visible radiation [6]. Doping with lanthanide ions such as Eu³⁺, Pr³⁺ and Yb³⁺ in TiO₂ was found to improve the photo-catalytic activity for the photo degradation of salicylic acid and t-cinnamic acid [7].

Sensitization of Cu doped TiO₂ with eosin improved the photo-catalytic activity for water splitting under visible light irradiation [8]. Doping TiO₂ with 0.1 % Nd and impregnation with Pt produced enhanced photo-catalytic activity for water splitting due to the prevention of phase transformation of TiO₂ from anatase to rutile and inhibition of particle growth [9].

Zhang and Liu [10] found cerium doping could prohibit the recombination of the photogenerated electron–hole pairs.

✉ Behzad Koozegar Kaleji
b.kaleji@malayeru.ac.ir; bkaleji@yahoo.com

¹ Department of Materials Engineering, Faculty of Engineering, Malayer University, Malayer, P.O. Box: 65719-95863, Iran

² Material and Energy Research Center (MERC), Karaj, P.O. Box: 31878-316, Iran

Yan et al. [11] reported preparation of Ce-doped titania through sol–gel auto-igniting process. It exhibited strong absorption in the UV–Vis range and a red-shift in the band-gap transition. However it was also reported that superfluous dopants would act as recombination center [12].

In the present study, Sn and Ce have been selected as co-dopants to increase the photo-catalytic activity of TiO₂ at the visible light wavelengths. Sn/Ce co-dopants, not reported in earlier studies were used during preparation process. The nanopowders were synthesized by sol–gel process. The effect of the dopant cations on the structure and the optical properties was studied in a through process. The efficiency of these samples as photocatalysts for the decomposition of MB solution, as an organic compound model, under visible excitation was investigated.

2 Experimental procedures

2.1 Preparation of Ce/Sn co-doped TiO₂ nanoparticles

The preparation of precursor solution for Sn/Ce co-doped TiO₂ nanoparticles is described as follows: titania, tin oxide and ceria sols were prepared, separately. For the preparation of TiO₂ sol, titanium (IV) butoxide (TBT = Ti(OC₄H₉)₄, Aldrich) was selected as titanium source. First, 0.35 mol ethanol (EtOH, Merck) and 0.04 mol ethyl acetoacetate (EAcAc is as a sol stabilizer during preparation of sol, Merck) were mixed, and then 0.01 mol TBT was added by the rate of 1 ml/min to the mixture at the ambient temperature (25 °C). The solution was continuously stirred for 45 min, followed by the dropping of HNO₃ as catalyst to the solution until pH of 3. De-ionized water was added to the solution slowly to initiate hydrolysis process. Solution was aged for 24 h in order to complete all reactions. The chemical composition of the resultant alkoxide solution was TBT: H₂O: HNO₃: EAcAc: EtOH = 1: 10: 1: 4: 35 in molar ratio. In order to prepare tin oxide sol and ceria sol, stannous chloride (SnCl₂·2H₂O, Merck) and cerium nitrate hexahydrate (Ce(NO₃)₃·6H₂O, Merck), were dissolved in EtOH with molar ratio of SnCl₂·2H₂O: EtOH = 1:35 and Ce(NO₃)₃·6H₂O: EtOH = 1:35 at ambient temperature with continuous stirring. Solutions were aged for 24 h in order to complete all reactions. Then, mixtures of TiO₂, tin oxide, and ceria sol were made with different mol percent of Ce and Sn at the ambient temperature. Samples were dried at 100 °C for 1 h and finally heated at a rate of 5 °C/min and calcined at 475 °C for 1 h in air atmosphere. The final product were molar content of Ce and Sn, that Ce was set to change from 0.5, 1.0, 2.0 mol% and Sn was set to change from 1, 5, 10 mol%.

2.2 Characterization methods

Differential thermal analysis (DTA) and thermogravimetric (TG) were used in order to determine crystallization temperature with a heating rate of 10 °C/min (STA 1460 equipment). Phase identification of nanopowders were recorded using X-ray diffraction (XRD) analysis (Philips, MPD-XPRT, λ: Cu_{kα} = 0.154 nm). The samples were scanned in the 2θ range of 20°–70°. Morphology of the nanopowders was observed using field emission scanning electron microscopy (FE-SEM, XL30 Series) with an accelerating voltage of 10–15 kV. Morphology of the nanopowders was observed using Transmission electron microscopy (TEM, Zeiss-EM10C-80 kV).

X-ray photoelectron spectroscopy (XPS) spectra were recorded using a PHI 5000C ESCA spectrometer equipped with Mg K_α radiation (hν = 1253.6 eV). The pressure of the analyzer chamber was maintained at 5 × 10⁻⁸ Pa. Spectra were calibrated with respect to the C1s peak at 284.6 eV.

N₂ adsorption–desorption isotherms were determined in a surface analyzer equipment (BEL Japan Inc., Osaka, Japan) at 77 K. BET surface area and BJH analyses were used to determine the total specific surface area and the pore size distribution.

2.3 Photo-catalytic activity measurement

The photo-catalytic activity of Ce/Sn co-doped TiO₂ was evaluated by decomposing aqueous MB solution (10 ppm) under Visible light. Before photo-catalytic decomposition experiment, the suspension of MB and photocatalyst was magnetically stirred in dark for 30 min to achieve adsorption/desorption equilibrium. Visible irradiation was provided by xenon lamp (500 W) equipped with a cutoff filter to remove light with wavelength below 400 nm. In a typical experiment, 0.08 g of doped TiO₂ was dispersed in aqueous MB solution. At given irradiation time (1 h), the samples (3 ml) were taken out and analyzed by UV–Vis spectrophotometer (WinAspect-Spekol-Analytik jena AG). The intensity of the MB characteristic band at 664 nm (I₆₆₄: the main absorption band of MB) in the obtained UV–Vis spectrum was used to determine the absorption of MB in the solution (A_t). The degradation rate of MB, which represents the photo-catalytic efficiency of the nanoparticles, can be determined by Eq. (1).

$$\eta(\%) = (A_0 - A_t)/A_0 \times 100 \quad (1)$$

where η is degradation rate, A_t is absorption after radiation and A₀ is absorption before radiation [13].

3 Results and discussion

3.1 TG–DTA analysis of titania based precursor gel

TiO₂ sol was heated for 1 h at 100 °C for gel formation. TG–DTA curve of TiO₂ gel (titania based precursor gel) from ambient temperature up to 700 °C is shown in Fig. 1. The sample lost weight gradually with the increase of temperature until about 600 °C. After 600 °C the change in weight was insignificant. The total weight loss was about 27.7 % of the original sample weight. Also, curves shows an endothermic peak at 92 °C (50–100 °C) which is attributed to evaporation of absorbed water and solvent (EtOH) from the gel. The first exothermic peak at 129 °C (120–140 °C) is probably attributed to combustion of residual organic component of TBT precursor. It is clear that titania precursor gel is thermally stable from 140 °C up to 280 °C. Small exothermic peak at temperature of 298 °C (290–340 °C) is probably corresponds to combustion of EAcAc (auto ignition temp. = 295 °C). The curve contains two exothermic peaks, first at about 400–470 °C related to the crystallization of anatase phase of TiO₂ and at 495 °C (460–520 °C) which is related to the phase transformation of anatase to rutile [14, 15].

3.2 XRD analysis of Sn/Ce co-doped TiO₂ nanoparticles

Figure 2 shows the XRD patterns of the nanoparticles with Sn and Ce doped samples calcined at 475 °C for 1 h. The peaks at 25.3°, 37.7°, 48.1°, 53.8°, and 55.1° in all doped samples belongs to (101), (004), (200), (105), and (211) planes of anatase phase of TiO₂. In addition, broad peaks due to rutile TiO₂ are also observed at 27.4° and 36.1°. All nanoparticles (Table 1: TSC6, 7, 8, 9) were identified as polymorphs of anatase (JCPDS: No. 21-1272) and rutile (JCPDS: No. 21-1276), without any significant impurity

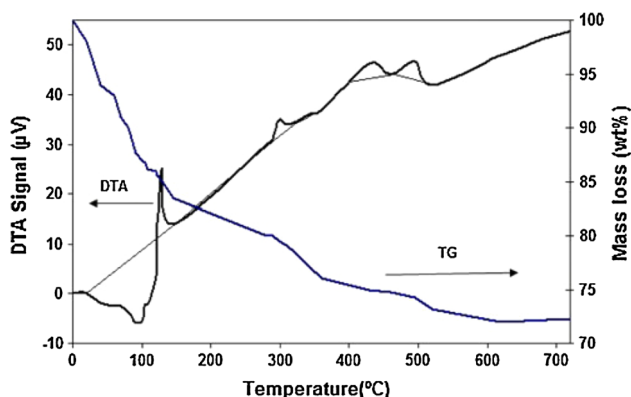


Fig. 1 DTA curve of the gel (titania based precursor gel) from ambient temperature up to 700 °C (heating rate = 10 °C/min)

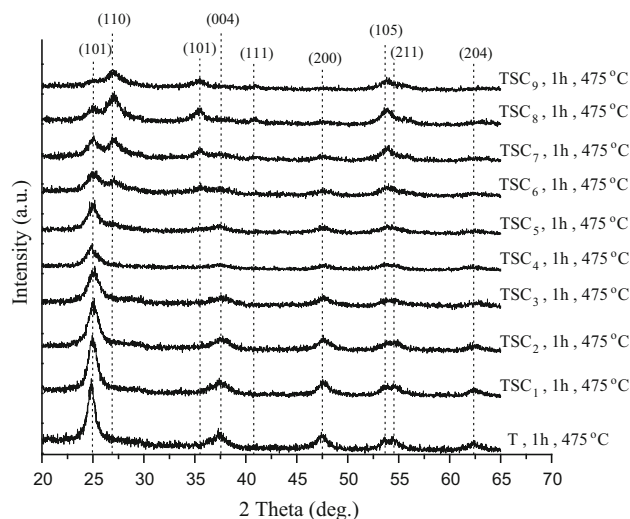


Fig. 2 XRD spectra of the pure (T) and doping TiO₂ nanopowders (TSC) calcined at 475 °C for 1 h. (The peaks at 25.3°, 37.7°, 48.1°, 53.8°, and 55.1° in all doped samples belongs to (101), (004), (200), (105), and (211) planes of anatase phase of TiO₂. In addition, broad peaks due to rutile TiO₂ are also observed at 27.4° and 36.1°.)

phases. Anatase appeared as the main phase and rutile crystallization was promoted by Sn⁴⁺ doping whilst inhibited by Ce⁴⁺ doping. In Sn/Ce co-doped sample no signs of metal or oxide phases of tin or cerium were detected which suggests the substitution of Sn⁴⁺ and Ce³⁺ in TiO₂ lattice [16, 17].

The average crystallite size of nanopowders (*d*) was determined from the XRD patterns, according to the Scherrer equation [18]. The values of FWHM and diffraction angle of anatase and rutile phases were calculated from anatase (1 0 1) and rutile (1 1 0) planes diffraction lines, respectively.

The amount of rutile in the samples (Table 1) was calculated using equation: [19]

$$X_R = (1 + 0.8I_A/I_R)^{-1} \quad (2)$$

where X_R is the mass fraction of rutile in the samples, and I_A and I_R are the X-ray integrated intensities of (1 0 1) reflection of the anatase and (1 1 0) reflection of rutile, respectively.

The diffraction peaks of crystal planes (101), (200), and (105) of anatase phase in XRD patterns were selected to determine the lattice parameters of the TiO₂ and doped TiO₂ nanopowders. The lattice parameters were obtained by using the Eq. (3) [13]

$$\begin{aligned} (\text{Bragg's law}) : 2d_{(hkl)} \sin \theta &= \lambda \\ (1/d_{(hkl)})^2 &= (h/a)^2 + (k/b)^2 + (l/c)^2 \end{aligned} \quad (3)$$

where $d_{(hkl)}$ is the distance between the crystal planes of (hkl); λ is the wavelength of X-ray used in the experiment; θ is the diffraction angle of the crystal plane; h, k and l are

Table 1 Summary of physical properties of prepared undoped (T) and Sn/Ce co-doped TiO₂ (TSC) samples

Sample code	%Ce	%Sn	%A	%R	d _A (nm)	d _R (nm)	a = b (Å)	c (Å)	V _{u.c} (Å) ³	BET (m ² /g)
T	–	–	100	–	21.8	—	3.822	10.610	155.717	71.48
TSC1	0.5	1	100	–	15.7	—	3.489	9.671	117.726	99.20
TSC2	1	1	100	–	13.1	—	3.859	9.595	142.907	118.15
TSC3	2	1	100	–	11.8	–	3.859	9.613	143.155	131.51
TSC4	0.5	5	100	–	12.9	–	3.774	9.541	135.902	120.25
TSC5	1	5	100	–	12.6	–	3.801	9.802	141.615	123.48
TSC6	2	5	62	38	10.5	14.8	3.801	9.528	137.656	122.73
TSC7	0.5	10	29	71	9.5	14.5	4.411	5.974	116.235	110.68
TSC8	1	10	20	80	8.8	13.2	4.399	5.810	112.430	116.58
TSC9	2	10	39	69	5.1	15.1	4.398	6.003	116.112	109.02

the crystal plane index; and *a*, *b*, and *c* are lattice parameters (in anatase form, *a* = *b* ≠ *c*).

The characteristic of all samples after calcination at 475 °C is reported in Table 1. By increasing Sn dopant, transformation of anatase to rutile phase was promoted, the amount of rutile phase structure was increased, and a decrease in the crystallite size was detected.

This decrease can be attributed to the presence of Sn–O–Ti and Ce–O–Ti in the Sn/Ce co-doped TiO₂ nanoparticles which inhibits the growth of crystal grains [20]. It is obvious that the lattice parameters and cell volume of the doped TiO₂ nanoparticles increased by Sn an Ce substitution with Ti⁴⁺ in titania lattice.

The crystalline degree of TiO₂ decreased by co-doping as indicated by the broader appearance of the main anatase peak at 25.3° (Fig. 2 or Table 1). For, the presence of Sn⁴⁺ or Ce³⁺ ions permits the rearrangement of Ti⁴⁺ and O²⁻ ions in the lattice in co-doped TiO₂ which promoted the anatase to rutile phase transformation [21].

Low concentration doping of Sn (1 mol%) is not sufficient for rutile phase development. The diffraction peaks of rutile crystallites appeared in X-ray patterns with increasing Sn dopant in samples. The addition of Sn has a promoting effect on the transformation of anatase to rutile crystalline phase [22, 23], due to the rutile like structure of SnO₂-cassiterite phase. It was found that the (1 0 1) anatase and (1 1 0) rutile plane peak positions shift to smaller diffraction angles with increasing Sn content in TiO₂ nanoparticles, which resulted from the substitution of Ti with Sn in the TiO₂ lattice. For pure TiO₂, the anatase crystallite size decreases with increasing molar percentage of Sn and Ce. The lattice parameters and cell volume of the pure and doped TiO₂ nanopowders are reported in Table 1. The lattice parameters and cell volume of the doped TiO₂ nanopowders increase with increasing Sn and Ce substitution with Ti⁴⁺ in titania lattice. Based on the trend seen

in Table 1, surface area of the co-doped TiO₂ increased with both Sn and Ce content relative to pure TiO₂.

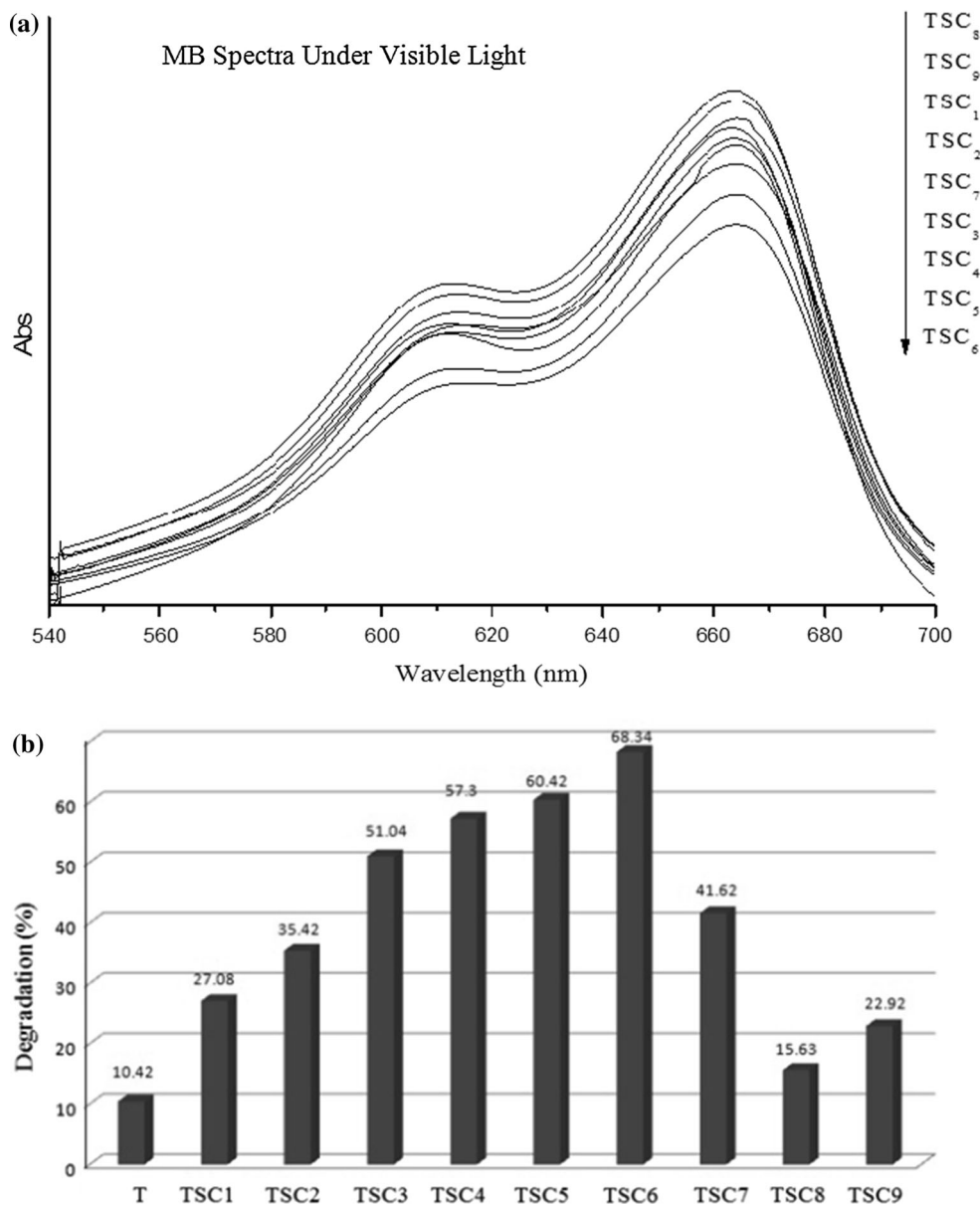
3.3 UV–Vis analysis of co-doped samples

Figure 3 shows the results of photo-catalytic decomposition of MB solution caused by direct contact with nanopowders doped with Sn and Ce at different concentrations (according to Table 1). The order of photo-catalytic activity of TiO₂ nanopowders at 1 h under visible irradiation was as follows: TSC6 > T, which suggests that doping enhanced the photo-catalytic activity of TiO₂. This enhanced photo-catalytic activity is due to suppressed recombination of photo generated electrons and holes. As mentioned, a mixture of anatase and rutile phase which is higher than (TSC6 (A % = 62, R % = 38 %) sample relative to another samples) shows higher photo-catalytic activity (least absorption).

Anatase has greater tendency to combine with organic compounds and their high degradation rate and recombination of electrons-holes at this phase which acted as a suitable photo-catalytic material. MB solution had the lowest amount of absorption at presence of TSC6. other samples represented the higher level of decomposition.

Figure 3b shows that the about 69 % of MB was decomposed in the presence of TSC6 after visible irradiation for 1 h, while the values in the presence of T is about 10 %, and highest irradiation induced degradation of MB is for the TCS6 sample. By introducing Sn and Ce to TiO₂ nanopowders, the TiO₂ nanocomposite changed from pure TiO₂ nanopowders in both physical and chemical characteristics, such as phase structure, surface areas, crystallite size (Table 1), and chemical compositions. Thus, the TSC6 sample calcined at 475 °C have higher crystallization and intensity than anatase phase which is due to the increase in photo-catalytic activity [24].

Fig. 3 **a** Photo-catalytic decomposition profile of MB over different Sn/Ce co-doped TiO₂ nanoparticles calcined at 475 °C for 1 h, **b** Photo-catalytic degradation of MB determined by pure and doped TiO₂ nanopowders after 1 h visible irradiation



3.4 XPS and BET analysis

XPS is a highly sensitive technique of surface analysis, and is an effective method to investigate the surface composition and chemical states of solid samples. XPS measurements were carried out to determine the surface composition and chemical state of Sn/Ce co-doped TiO₂ nanoparticles calcined at 475 °C. XPS images for a selected sample (TSC6) are shown in Fig. 4. The XPS spectrum in Fig. 4a indicates the presence of titanium, oxygen, carbon, tin, and cerium on the surface. All the binding energies were referenced to the C 1s peak at 284.6 eV. The binding energy of Ti 2p_{3/2} and Ti 2p_{1/2} were observed at approximately 458.1 and 463.5 eV,

respectively (Fig. 4b), indicating that the Ti element mainly existed with the chemical state of Ti⁴⁺ [22, 25]. XPS spectra of Sn 3d region are given in Fig. 4c. Two peaks corresponding to Sn 3d_{5/2} (486.9 eV) and Sn 3d_{3/2} (494.4 eV) were observed. The peak position corresponding to Sn 3d_{5/2} is located between those of Sn 3d_{5/2} in SnO₂ (487.5 eV) and Sn 3d_{5/2} in metallic Sn (485.0 eV), which is ascribed to incorporated Sn⁴⁺ in the lattice of TiO₂ [22, 26]. XPS spectra of Ce 3d region are given in Fig. 4d. The spectra for the Ce 3d are rather complex because of the hybridization of Ce 3d and Ti 2p orbitals and splitting of the peaks. According to the previous reports, the spectra are divided into 6 peaks related to the presence of both Ce³⁺ and Ce⁴⁺ [27, 28]. The presence of both Ce³⁺ and

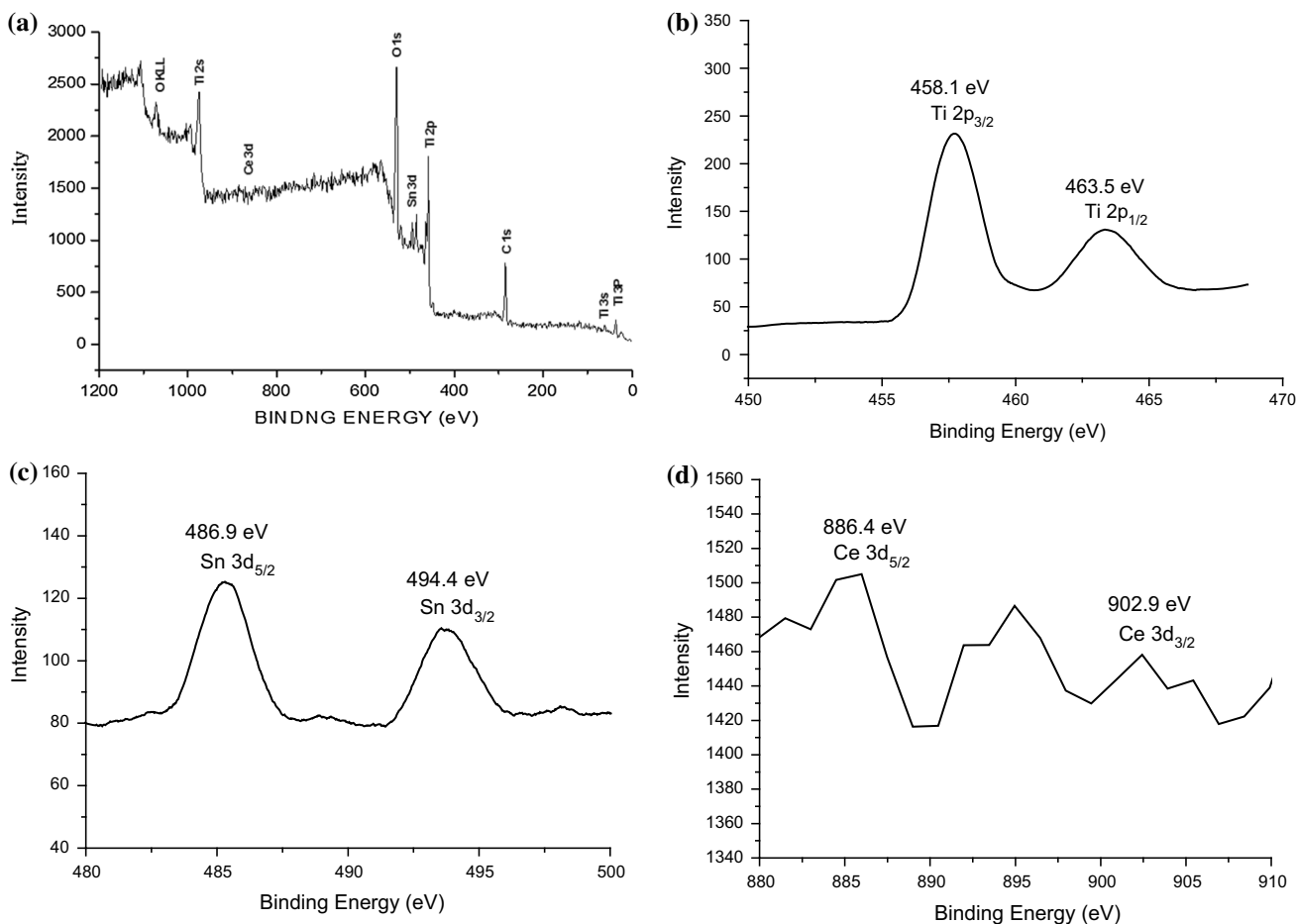


Fig. 4 XPS analysis of calcined Sn/Ce co-doped TiO₂ nanoparticles (TSC6) **a** survey analysis (Broad scan), **b** Ti 2p, **c** Sn 3d, **d** Ce 3d

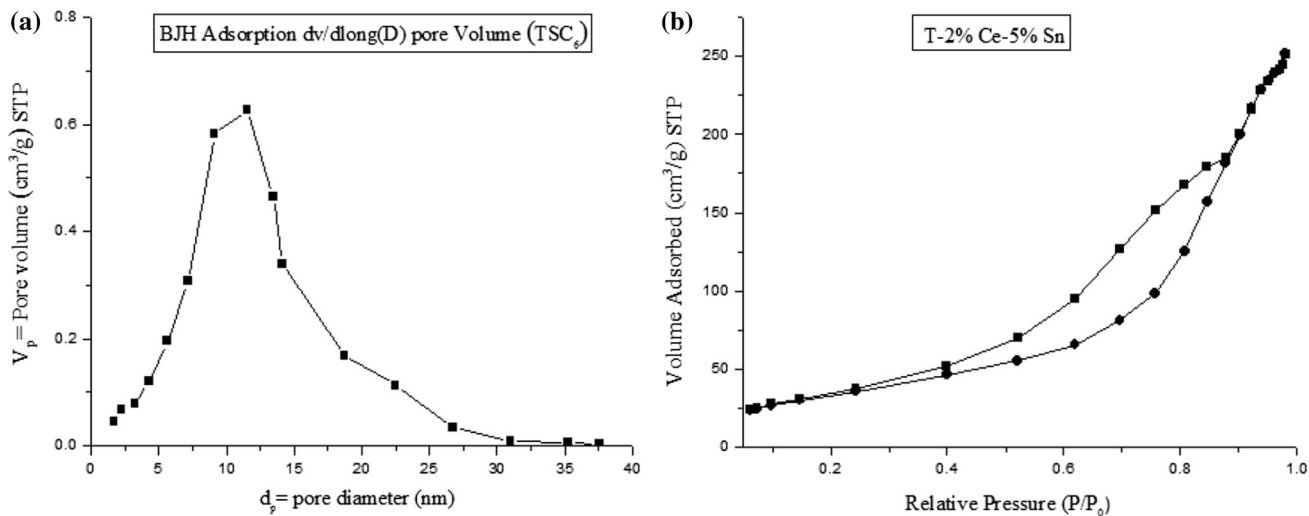


Fig. 5 Nitrogen adsorption–desorption isotherm (TSC6)

Ce⁴⁺ showed that the surface of the catalyst was not fully oxidized, thus indicating the existence of some oxygen vacancies. Because of the complexity of the spectra, it is

difficult to indicate the exact percentage of the each oxidation state for the Ce. The spectra showed a very small peak around 882 eV and two broad peaks around 902.9 and

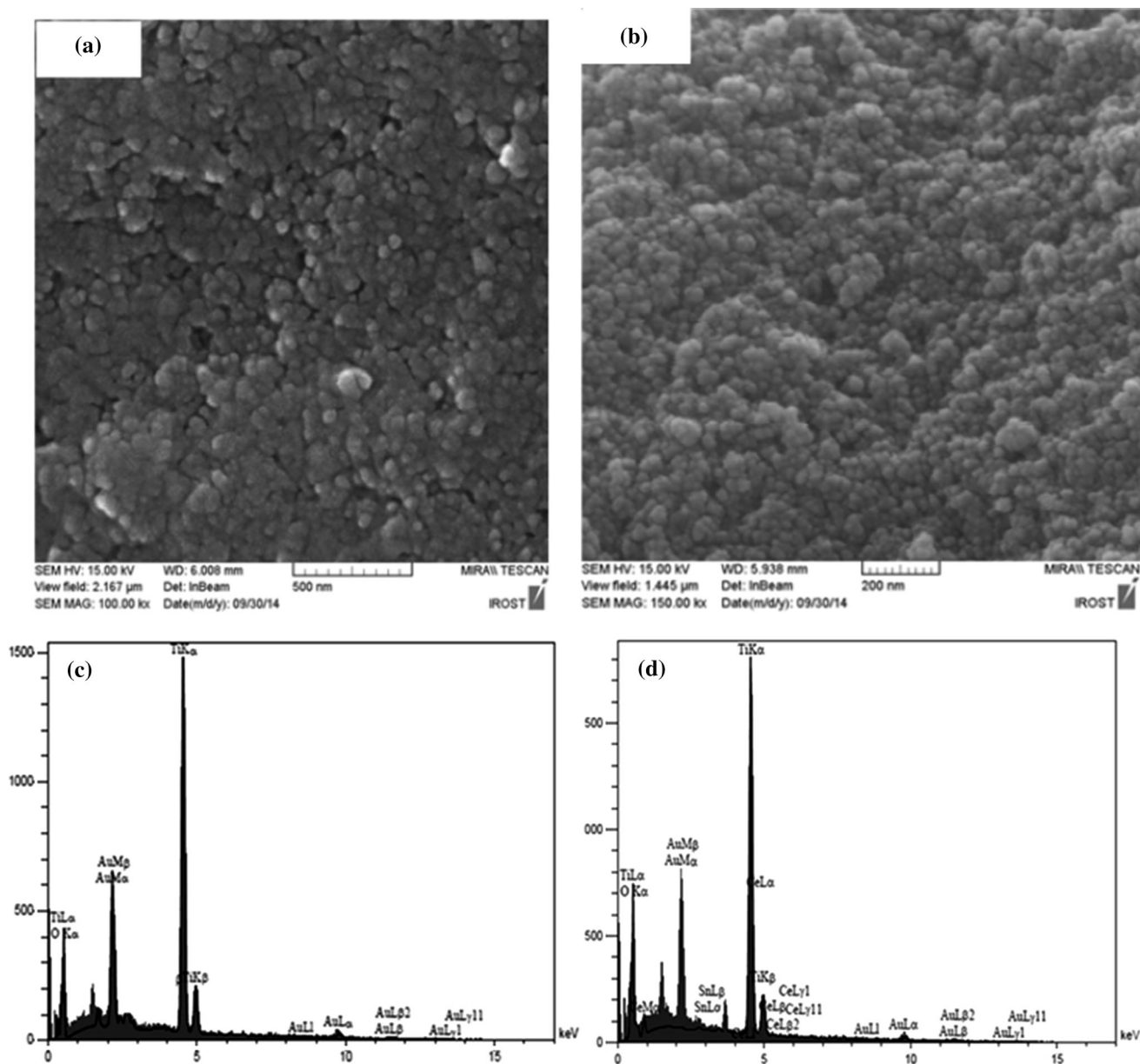


Fig. 6 FE-SEM and EDX micrographs of sample calcined at 475 °C for 1 h, **a** and **c** pure TiO₂ (T), **b** and **d** TSC6

886.5 eV, which indicates the presence of Ce³⁺ in a greater percentage than the Ce⁴⁺ in the sample [28, 29]. This was helpful in the shifting of the absorption toward the visible region as well as beneficial for the enhancement of the photo-catalytic performance of the catalyst.

The nitrogen adsorption–desorption isotherm at 77 K and the BJH pore size distribution of sample (TSC6) calcined at 475 °C are showed in Fig. 5a, b. the sample exhibited the classical shape of a type IV isotherm according to the IUPAC classification, typical for mesoporous solids [30, 31]. The existence of the hysteresis loop in the isotherms is due to the capillary condensation of N₂ gas occurring in the mesopores.

The surface area and the mean pore diameter of co-doped nanoparticles calcined at 475 °C are 122.73 m²/g and 11.7 nm, respectively.

3.5 FE-SEM, EDX and TEM analysis

Typical FE-SEM results of undoped (T) and co-doped TiO₂ (TSC6) samples are shown in Fig. 6. In comparison with the pure TiO sample (Fig. 6a, 20–50 nm in diameter), the co-doped (Fig. 6b) have relatively small particle size (about 10–20 nm in diameter), narrow size distribution, and uniform dispersion, indicating that the co-doping can

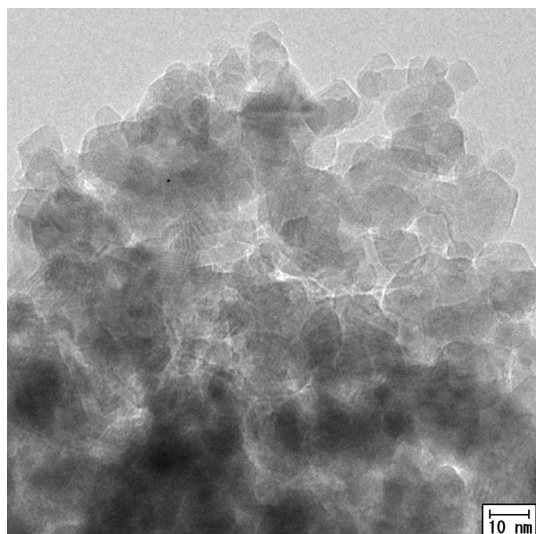


Fig. 7 TEM micrograph of TSC6 calcined at 475 °C for 1 h

improve the particle morphology, and prevented the grain growth of TiO_2 during heat-treatments.

The quantitative analysis of pure and Sn/Ce co-doped TiO_2 nanoparticles were determined by Energy dispersive X-ray (EDX) study, which revealed the presence of Ti and O as elementary components (Fig. 6c). There are two strong peaks corresponding to Ti and O which confirms the presence of pure TiO_2 phase [32]. The typical EDX spectra of TSC6 nanoparticles are shown in Fig. 6d which indicates presence of Ti, Sn, Ce, and O as elementary Fig. 7 components.

Figure 7 shows the typical TEM images of TSC6 nanoparticles (best photocatalytic activity), indicating that they are highly sensitive to the focused electron beams during TEM observation. A series of aggregation spheres with about 20 nm in diameter are shown in. It can be seen that the primary crystallite size is about 12 ± 1 nm (Fig. 7), which is in agreement with the value of the crystallite size determined by XRD (as shown in Table 1).

4 Conclusion

In this research, Sn/Ce co-doped TiO_2 nanoparticles with photo-catalytic properties have been prepared by sol–gel method. The photo-catalytic activity of the co-doped nanoparticles (TSC) were higher than pure TiO_2 nanoparticle (T). Sn^{4+} and Ce^{3+} substitution with Ti^{4+} in the titania lattice results in a decrease in the rate of photo-generated electron–hole recombination, which caused the enhancement in photo-catalytic degradation rate. The anatase–rutile phase transformation was promoted by Sn^{4+} and inhibited by Ce^{3+} doping. Photo-catalytic

activity of the co-doped nanoparticles under visible irradiation was improved comparing to undoped nanoparticles.

References

1. F. Caimei, X. Peng, S. Yanping, J. Rare. Earth. **24**, 309 (2006)
2. V. Stengl, S. Bakardjieva, N. Murafa, Mater. Chem. Phys. **114**, 217 (2009)
3. X. Chen, S.S. Mao, Chem. Rev. **107**, 2891 (2007)
4. S.R. Shirsath, D.V. Pinjari, P.R. Gogate, S.H. Sonawane, A.B. Pandit, Ultrason. Sonochem. **20**, 2771 (2013)
5. Q. Chen, D. Jiang, W. Shi, D. Wu, Y. Xu, Appl. Surf. Sci. **255**, 7918 (2009)
6. H. Kato, A. Kudo, J. Phys. Chem. B. **106**, 5029 (2002)
7. K.T. Ranjit, I. Willner, S.H. Bossmann, A.M. Braun, J. Catal. **204**, 305 (2001)
8. C.C. Vidyasagar, Y. Arthoba Naik, T.G. Venkatesha, R. Viswanatha, Int. J. Nanomater. Biostruct. **2**(3), 34 (2012)
9. H. Cuiying, Y. Wansheng, D. Ligin, L. Zhibin, S. Zhengang, Z. Lancui, Chin. J. Catal. **27**, 203 (2006)
10. X. Zhang, Q. Liu, Mater. Lett. **62**, 2589 (2008)
11. Q.Z. Yan, X.T. Su, Z.Y. Huang, C.C. Ge, J. Eur. Ceram. Soc. **26**, 915 (2006)
12. A.D. Paola, E. Garcia-López, S. Ikeda, G. Marci, B. Ohtani, L. Palmisano, Catal. Today **75**, 87 (2002)
13. R.W. Baker, *Membrane Technology and Application* (Wiley, Chichester, 2004)
14. B. Guo, Z. Liu, L. Hong, H. Jiang, Surf. Coat. Technol. **198**, 24 (2005)
15. A. Verma, S.B. Samanta, A.K. Bakhshi, S.A. Agnihotry, Sol. Energy Mater. Sol. Cells **88**, 47 (2005)
16. J. Lu, L.P. Bauermann, P. Gerstel, U. Heinrichs, P. Kopold, J. Bill, F. Aldinger, Mater. Chem. Phys. **115**, 142 (2009)
17. N. Yan, Z. Zhu, J. Zhang, Z. Zhao, Q. Liu, Mater. Res. Bull. **47**, 1869 (2012)
18. T. Tong, J. Zhang, B. Tian, F. Chen, M. Anpo, J. Colloid Interface Sci. **315**, 382 (2007)
19. P. Klug, L.E. Alexander, *X-Ray Diffraction Procedures* (Wiley, New York, 1974)
20. R.A. Spurr, H. Myers, Anal. Chem. **29**, 760 (1957)
21. F. Sayilkana, M. Asiltürka, N. Kirazb, J. Hazard Mater. **162**, 1309 (2009)
22. B. Koozegar Kaleji, Sol–Gel Sci. **67**, 312 (2013)
23. K.N.P. Kumar, D.J. Fray, J. Nair, F. Mizukami, T. Okubo, Scr. Mater. **57**(8), 771 (2007)
24. N. Najibi, N. Ilkhechi, B. Koozegar Kaleji, D. Fallah, Opt. Quant. Electron. **47**, 633 (2015)
25. R. Sanjines, H. Tang, H. Berger, F. Gozzo, G. Margaritondo, F. Levy, J. Appl. Phys. **75**, 2945 (1994)
26. Y. Cao, W. Yang, W. Zhang, G. Liu, P. Yue, New J. Chem. **28**, 218 (2004)
27. F. Larachi, J. Pierre, A. Adnot, A. Bernis, Appl. Surf. Sci. **195**, 236 (2002)
28. X. Sun, H. Liu, J. Dong, J. Wei, Y. Zhang, Catal. Lett. **135**, 219 (2010)
29. M. Nasir, Z. Xi, M. Xing, J. Zhang, F. Chen, B. Tian, S. Bagwasi, J. Phys. Chem. C **117**, 9520 (2013)
30. J.C. Yu, L. Zhang, Z. Zheng, J. Zhao, Chem. Mater. **15**, 2280 (2003)
31. J. Xiao, T. Peng, R. Li, Z. Peng, C. Yan, J. Solid State Chem. **179**, 1161 (2006)
32. J.K. Yan, K.Y. Kang, G.Y. Gan, Mater. Des. **99**, 155 (2016)